



## ABSTRACT

8 A negative shortwave cloud feedback associated with higher extratropical liquid water content in  
9 mixed-phase clouds is a common feature of global warming simulations, and multiple mechanisms  
10 have been hypothesized. A set of process-level experiments performed with an idealized global cli-  
11 mate model show that the common picture of the liquid water path (LWP) feedback in mixed-phase  
12 clouds being controlled by the amount of ice susceptible to phase change is not robust. Dynamic  
13 condensate processes—rather than static phase partitioning—directly change with warming, with  
14 varied impacts on liquid and ice amounts. Here, three principal mechanisms are responsible for  
15 the LWP response, namely higher adiabatic cloud water content, weaker liquid-to-ice conversion  
16 through the Bergeron-Findeisen process, and faster melting of ice and snow to rain. Only melting  
17 is accompanied by a substantial loss of ice, while the adiabatic cloud water content increase gives  
18 rise to a net increase in ice water path (IWP) such that total cloud water also increases without an  
19 accompanying decrease in precipitation efficiency. Perturbed parameter experiments with a wide  
20 range of climatological LWP and IWP demonstrate a strong dependence of the LWP feedback on  
21 the climatological LWP and independence from the climatological IWP and supercooled liquid  
22 fraction. This idealized setup allows for a clean isolation of mechanisms and paints a more nuanced  
23 picture of the extratropical mixed-phase cloud water feedback than simple phase change.

## 24 **1. Introduction**

25 With atmospheric warming from greenhouse gases, cloud properties would vary in manifold  
26 ways, resulting in further changes in radiative fluxes and climate. Despite the recent advances  
27 in mechanistic understanding, the so-called cloud feedback is widely considered to be the largest  
28 contributor to the uncertainties in climate sensitivity and model projection of future warming  
29 (Sherwood et al. 2020). Ceppi et al. (2017) identifies three robust components of cloud feedback  
30 in comprehensive global climate models (GCMs): a positive longwave feedback from rising free  
31 tropospheric clouds, a positive shortwave (SW) feedback from decreasing subtropical low cloud  
32 fraction, and a negative SW feedback from increasing extratropical cloud optical depth.

33 Uncertainty associated with cloud feedback is dominated by the SW components (Soden and  
34 Vecchi 2011; Vial et al. 2013). Among these, this study focuses on the component that affects  
35 radiation through altering cloud optical depth or brightness (as opposed to cloud fraction). This  
36 cloud optical depth feedback is robustly negative in the Coupled Model Intercomparison Project  
37 Phase 5 (CMIP5) GCMs (Zelinka et al. 2016), though it may be artificially tuned to a small range  
38 (McCoy et al. 2016), and mechanistic uncertainty still abounds (Gettelman and Sherwood 2016;  
39 Ceppi et al. 2017; Korolev et al. 2017). Observations have shown that in pure liquid and mixed-  
40 phase (M-P, liquid and ice co-existing) clouds, cloud optical depth is primarily controlled by liquid  
41 water path (LWP), which is the vertically integrated cloud liquid (Stephens 1978). Ice affects cloud  
42 optical depth to a lesser extent owing to larger sizes of ice particles and ice water path (IWP) being  
43 generally smaller than LWP (McCoy et al. 2014; Cesana and Storelvmo 2017). GCMs predict a  
44 robust extratropical LWP increase in response to global warming, which is thought to be the main  
45 driver of the negative SW cloud feedback (e.g. Ceppi et al. 2016).

46 Recent modeling studies have highlighted the need to improve GCM representation of the  
47 extratropical cloud feedback. Zelinka et al. (2020) showed that the increased climate sensitivity  
48 in CMIP6 models relative to CMIP5 is largely due to changes in this feedback. The multi-model  
49 ensemble mean changes from negative in CMIP5 to slightly positive in CMIP6 presumably due to  
50 model physics differences. Therefore, it is critical to delineate the underlying mechanisms of the  
51 extratropical cloud feedback and its various components.

52 Multiple pathways have been proposed to explain the extratropical increase (Ceppi et al. 2017) in  
53 liquid cloud condensate. The first is an increase in the adiabatic cloud water content. With warming,  
54 the amount of water condensed in saturated updrafts increases (Tselioudis et al. 1992; Gordon and  
55 Klein 2014); the fractional change is greater at colder temperatures (Betts and Harshvardhan 1987;  
56 Somerville and Remer 1984). The second mechanism involves phase change in M-P clouds (e.g.,  
57 McCoy et al. 2015; Storelvmo et al. 2015; Tan et al. 2018), which occurs only at temperatures  
58 below freezing. As isotherms shift upward with warming, liquid is presumed to replace ice,  
59 thereby increasing cloud optical depth. An implication of this phase change mechanism is that  
60 since liquid precipitates less efficiently than ice, total cloud water content may increase (Klein  
61 et al. 2009; McCoy et al. 2015; Ceppi et al. 2016; McCoy et al. 2018). This work will address  
62 both mechanisms and their impacts on LWP and IWP. A third potential mechanism frequently  
63 mentioned in the literature is poleward jet shifts. As this effect is highly model dependent and  
64 unlikely to be dominant (Ceppi and Hartmann 2015; Ceppi et al. 2016; Wall and Hartmann 2015),  
65 it is not explored here.

66 The relative importance of the proposed mechanisms is still unclear. LWP itself is robustly  
67 linked to temperature in both models and observations (Terai et al. 2019), hinting at the potential  
68 for emergent constraints on the negative SW cloud feedback (Ceppi et al. 2016). McCoy et al.  
69 (2016) noted that among CMIP5 GCMs, T5050, the diagnosed temperature at which liquid and

70 ice exists in equal amounts globally, is strongly anti-correlated with LWP, but positively correlated  
71 with cloud fraction despite the lack of a physical explanation. At the same time, the range of T5050  
72 estimated from space-borne observations is much lower than that diagnosed from CMIP5 models,  
73 suggesting that the models tend to freeze liquid at temperatures that are too high (Cesana et al. 2015;  
74 McCoy et al. 2016). Multiple GCM studies (McCoy et al. 2014; Tan et al. 2016; Frey and Kay 2018)  
75 have shown that increasing the ratio of supercooled liquid to total water (the so-called supercooled  
76 liquid fraction or SLF) in M-P clouds decreases the SW negative feedback, and thus increases  
77 climate sensitivity. These results have been attributed to models with higher T5050 having more  
78 susceptible ice (McCoy et al. 2018), which is hypothesized to control the feedback strength (as  
79 in Tan et al. 2018). Improvements in understanding the governing mechanisms are especially  
80 important as some modeling studies with observationally-based constraints have suggested that  
81 the negative SW cloud optical depth feedback is too strong or even of the wrong sign in GCMs,  
82 implying that the actual climate sensitivity may have been underestimated (e.g. Tan et al. 2016;  
83 Terai et al. 2016).

84 This work utilizes an idealized model to probe the physical mechanisms underlying the extrat-  
85 ropical cloud water feedback. Idealized models complement comprehensive GCMs (Held 2005,  
86 2014) since their workings are relatively easy to understand (Pierrehumbert et al. 2007). This  
87 is particularly true as previous studies of M-P clouds are hindered by the complexity of cloud  
88 microphysics and the fact that the physics and dynamics of M-P clouds are non-linear in GCMs  
89 (Morrison et al. 2011). We seek to test the plausibility of the leading hypotheses in the M-P cloud  
90 feedback literature including the simple conceptual picture of liquid increasing at the expense of  
91 ice with warming, which has fueled the notion of the extratropical LWP feedback being controlled  
92 by the amount of susceptible ice. As mentioned above, more ice in the control climate is thought  
93 to cause a greater increase in liquid with warming. The main supporting evidence is the positive

94 correlation between the LWP feedback and climatological SLF or T5050 (McCoy et al. 2018; Tan  
95 et al. 2018). With a set of targeted, process-level experiments, we seek to explore the complexity of  
96 the M-P cloud feedback. We also use a perturbed parameter ensemble of experiments with varied  
97 cloud physics settings to investigate the feasibility of predicting the LWP feedback from the control  
98 climate.

99 This paper is arranged as follows. Section 2 outlines the methodology. Section 3 presents the  
100 results from process-level and perturbed parameter experiments. Section 4 compares with previous  
101 studies with the goal of examining the plausibility of the phase change mechanism and other related  
102 arguments. Section 5 concludes as to rethinking the physical picture of the extratropical M-P cloud  
103 feedback and suggests a path for future research.

## 104 **2. Methodology**

105 The model used here is the Held-Suarez dry dynamical core (Held and Suarez 1994) with the  
106 addition of passive water vapor and cloud tracers (specific humidity, cloud liquid mixing ratio,  
107 cloud ice mixing ratio, and cloud fraction), whose evolution follows a prognostic large-scale cloud  
108 scheme with bulk single-moment microphysics (Ming and Held 2018). The sub-grid-scale total-  
109 water-based relative humidity (RH) is assumed to follow a beta distribution, which is a function  
110 of the grid-mean RH. The beta distribution is designed such that a grid box with a mean total-  
111 water-based RH value above a certain threshold value ( $RH_c$ , 83.3% at the default half-width of  
112 0.2) would have sub-grid-scale RH over 100%, thus producing clouds. There is no convective  
113 parameterization. The role of surface evaporation is mimicked by nudging air parcels below  
114 850 hPa toward saturation as in Galewsky et al. (2005). Clouds are completely decoupled from  
115 dynamics (i.e. no latent heating or cloud radiative effects), making this model a unique tool for  
116 isolating individual mechanisms in a clean fashion. The control simulation (Ctrl) is the model's

117 default climate. For Ctrl and all perturbation experiments, the atmospheric state (e.g. temperature  
118 and winds) is identical at every time step. All model simulations include a 300-day spin-up, and  
119 the next 1000 days are averaged for analysis.

120 The bulk microphysics scheme has separate but interconnected treatments of liquid and ice  
121 based on Rotstayn (1997) and Rotstayn et al. (2000). The same scheme is also used in the GFDL  
122 AM2.1 model, one of the two models compared in Ceppi et al. (2016). As shown in Fig. 1, water  
123 vapor forms cloud liquid and ice through condensation and deposition, respectively. The initial  
124 partitioning of cloud liquid and ice is based entirely on temperature. All condensate at temperatures  
125 greater than  $-40^{\circ}\text{C}$  is formed as liquid based on the consideration that ice nuclei are generally limited  
126 in the atmosphere (Rotstayn et al. 2000). Supercooled liquid (existing between  $0^{\circ}$  and  $-40^{\circ}\text{C}$ ) can  
127 then be converted to ice through other processes such as the Bergeron-Findeisen (BF) process.  
128 In the control climate, the primary sink of water vapor (98.8% globally) is conversion to cloud  
129 liquid. Microphysical sources of water vapor come from cloud liquid (evaporation), cloud ice (ice  
130 sublimation), rain (rain evaporation) and snow (snow sublimation). Together, rain evaporation and  
131 snow sublimation, the most significant microphysical sources, comprise 22.3% of all water vapor  
132 sources. Surface evaporation (a non-microphysical source) constitutes the main supplier of water  
133 vapor (76.4%).

134 Cloud liquid forms rain through autoconversion and accretion. To facilitate conversion of cloud  
135 liquid to ice through the BF process, a minimum amount of ice crystal mass on which deposition  
136 can occur is assumed to be always present. (Note that the BF process is not formulated to be  
137 explicitly linked to aerosols.) Cloud liquid is also converted to cloud ice through riming (accretion  
138 of cloud liquid by ice) and homogeneous freezing (colder than  $-40^{\circ}\text{C}$ ). Overall, 68.2% of cloud  
139 liquid sinks are to rain and 30.9% to cloud ice.

140 Cloud ice is lost almost completely (98.3%) to snow through ice settling. In the microphysics  
141 scheme, cloud ice and snow are treated effectively as one species, experiencing the same fall rate,  
142 and are only distinguished by their location in or outside of a cloud. Ice and snow can melt into  
143 rain: if this takes place in a cloud, it is considered melting of ice; if it takes places outside of a  
144 cloud, it is considered melting of snow. Cloud ice is also lost to water vapor through sublimation.

145 The *process-level experiments* involve increasing the temperature field fed to certain parts of  
146 the microphysics scheme or the formulation of surface evaporation by 2 K (summarized in Table  
147 1). In the microphysics scheme, there are at least four explicitly temperature-dependent processes:  
148 partitioning of newly formed cloud condensate, the BF process, homogeneous freezing, and melting  
149 of ice and snow. When water vapor experiences condensation/sublimation at the beginning of the  
150 microphysics scheme, it is initially partitioned into cloud liquid and ice based solely on temperature.  
151 Only liquid is created at temperatures warmer than  $-40^{\circ}\text{C}$ , and only ice otherwise. Supercooled  
152 liquid can be converted to ice through the BF process, homogeneous freezing, and riming. For the  
153 BF process, temperature affects whether or not the process occurs (below  $0^{\circ}\text{C}$ ) as well as the rate  
154 of cloud liquid being converted to cloud ice, which is greater at lower temperatures (see Eqn. A8).  
155 These two effects are tested in combination (BF2K). (By contrast, riming is not directly dependent  
156 on temperature; see Eqn. A10.) Homogeneous freezing of cloud liquid to ice occurs only when  
157 the temperature is less than  $-40^{\circ}\text{C}$  and converts all cloud liquid to ice. Ice and snow melt into rain  
158 only when the temperature is higher than  $0^{\circ}\text{C}$ , with the melting being limited to the amount that  
159 would restore the grid-box temperature to  $0^{\circ}\text{C}$ . Melting of ice and snow are tested in combination  
160 (ME2K). All of these microphysical processes—initial partitioning, the BF process, homogeneous  
161 freezing, and melting—are also perturbed in tandem in MI2K.

162 A significant influence of temperature in the cloud scheme is in the calculation of the saturation  
163 specific humidity ( $q_s$ ) and related variables (the  $T$  derivative of  $q_s$ , the psychrometric constant, and

164 the sum of the vapor diffusion and thermal conductivity factors) that are used in many parts of the  
165 scheme. Since surface evaporation is also formulated in parallel based on  $q_s$ ,  $q_s$  for microphysics  
166 and surface evaporation are perturbed simultaneously in Qse2K. This experiment enables us to study  
167 the effect of the adiabatic cloud water content increase. Finally, to cover all the aforementioned  
168 effects of temperature as well as any other effects (such as the influence of temperature on air  
169 density), a 2-K temperature increase is fed to the entire cloud scheme and surface evaporation to  
170 create the Tse2K (full warming) experiment.

171 To develop a predictive theory of the extratropical M-P cloud feedback that is applicable to a wide  
172 range of control states, a set of *perturbed parameter experiments* (also summarized in Table 1) are  
173 created by systematically modifying three key parameters of the cloud scheme. The first two have  
174 been suggested as significant for the M-P cloud feedback: the strength of the BF process may too  
175 efficient (Tan et al. 2016) and  $RH_c$  too high (McCoy et al. 2016). To vary the strength of the BF  
176 process, the formula for the conversion rate is altered arbitrarily by multiplying with a constant  
177 (0.25, 0.5, 2 or 4). The corresponding experiments are labeled as quarBF, halvBF, doubBF and  
178 quadBF. Note that these adjustments do not result in actual changes in the BF rate as large as  
179 those imposed. The effective  $RH_c$  (83.3% in Ctrl) is varied from 76.7% to 90.0% at increments  
180 of  $\sim 3.3\%$  (rh767, rh800, rh867, and rh900) by altering the half-width of the sub-grid-scale RH  
181 beta distribution. Finally, a third parameter is chosen to cleanly affect the mean-state amount of  
182 cloud ice: the fall speed of cloud ice (relative to the large-scale vertical motion) is perturbed by  
183 multiplying with a constant (0.5, 0.75, 1.25 or 1.5). The corresponding experiments are v050,  
184 v075, v125 and v150. For each of these states, a Tse2K simulation (increasing the temperature  
185 field fed to the cloud scheme and surface evaporation by 2 K) is created, and the response (for  
186 example, rh767\_Tse2K minus rh767) analyzed.

187 The key to understanding the steady-state mixing ratios of cloud liquid and ice ( $q_l$  and  $q_i$ ,  
 188 respectively) and their responses to the warming is how they are related to the time tendencies of  
 189 the aforementioned microphysical processes. To illustrate the point, let us write the time derivative  
 190 of a variable  $q$  ( $q_l$  or  $q_i$ ) as:

$$\frac{dq}{dt} = s - aq^b, \quad (1)$$

191 where  $s$  is the source term, and the sink term is parameterized as a power-law function of  $q$  with  $a$   
 192 and  $b$  as constants. It follows that the fractional change of  $q$  can be related to the fractional change  
 193 of  $s$  by:

$$\frac{\delta q}{q} = \frac{1}{b} \frac{\delta s}{s}. \quad (2)$$

194 The formulation and behavior of the autoconversion parameterization (Eqn. A1) are discussed  
 195 in Golaz et al. (2011) (see their Equations 12-14). Although the rate is nominally proportional  
 196 to  $q_l^{7/3}$ , it is effectively controlled by a numerical limiter (Eqn. A3), which tends to set  $q_l$  at a  
 197 critical value ( $q_{crit}$ ) determined by a tunable threshold droplet radius ( $r_{thresh}$ ) and droplet number  
 198 concentrations ( $N$ ). Since neither  $r_{thresh}$  nor  $N$  changes in this study,  $q_l$  should be close to  $q_{crit}$   
 199 when autoconversion is the dominant process. By contrast, accretion is proportional to  $q_l$  and the  
 200 flux of rain (Eqn. A4). The BF rate (Eqn. A8) is effectively independent of  $q_l$ , but conditionally  
 201 proportional to  $q_i^{1/3}$ . Riming (Eqn. A10) is proportional to  $q_l$  and the flux of settling ice, which is  
 202 related to the fall speed and  $q_i$ . Similarly, ice settling (Eqn. A6) at a specific level is determined  
 203 by the fall speed and vertical gradient of  $q_i$  ( $\partial q_i / \partial p$ , where  $p$  denotes pressure). If  $q_i$  is altered by  
 204 the same ratio throughout the column, an assumption that holds approximately for the simulations  
 205 examined here, the fractional change in the ice settling rate would be the same as that in  $q_i$ . The  
 206 microphysical tendency equations are listed in the Appendix for reference. Condensation and  
 207 deposition, the main sources of cloud liquid and ice, are not directly related to  $q_l$  or  $q_i$ .

208 The analysis focuses on two variables: LWP and IWP, which are, respectively, vertically inte-  
209 grated cloud liquid and cloud ice in units of  $\text{g m}^{-2}$ . Absolute and fractional changes in LWP and  
210 IWP are normalized by warming and thus given in units of  $\text{g m}^{-2} \text{K}^{-1}$  and  $\% \text{K}^{-1}$ , respectively.  
211 Due to the highly simplified nature of the boundary layer in this model (i.e., surface evaporation  
212 saturating the air below 850 hPa), for the purposes of this analysis the vertical integral has a lower  
213 boundary of 850 hPa such that LWP and IWP only represent the cloud condensate above 850 hPa.  
214 Similarly, specific humidity and cloud condensate tendency terms, when column-integrated, only  
215 represent values above 850 hPa.  $30^\circ$  to  $60^\circ$  and  $60^\circ$  to  $90^\circ$  are considered the mid-latitudes and  
216 high-latitudes, respectively, and together they are considered the extratropics. Data is averaged  
217 between the two hemispheres because of the hemispheric symmetry of the simulated climate. The  
218 supercooled liquid fraction (SLF) is calculated as the ratio of cloud liquid to total cloud water  
219 (liquid and ice). The daily SLF is binned as a function of temperature at an interval of 0.1 K  
220 for each grid box in the extratropical region above 850 hPa with the temperature at which SLF is  
221 closest to 50% considered to be T5050 (liquid and ice partitioned equally).

### 222 3. Results

#### 223 *a. Process-level Experiments*

224 Fig. 2 shows the zonal-mean LWP and IWP in the control case (Ctrl), yielding a picture of the  
225 model's default climate [see Ming and Held (2018) for other related variables including RH and  
226 CF]. In the mid-latitudes, LWP and IWP are of comparable magnitude, with LWP being greater  
227 equatorward of the storm tracks (at around  $45^\circ$ ). In the total warming experiment (Tse2K), the  
228 general features, including the location of the storm tracks, remain the same. Both LWP and IWP

229 are higher at all latitudes in the warmer climate. The increase in LWP is more pronounced than  
230 that in IWP in the mid-latitudes, while they are more comparable in the high-latitudes.

231 Table 2 and Fig. 3 break down the LWP and IWP feedbacks seen in Tse2K. The increase in  
232 LWP (Fig. 3a) in the extratropics is dominated by the microphysical component (MI2K) with a  
233 much smaller (slightly less than 20%) contribution from the increased  $q_s$  (Qse2K). MI2K and  
234 Qse2K combine nearly linearly to produce the full Tse2K increase in LWP suggesting that Tse2K  
235 does not add any significant temperature-affected processes beyond those perturbed in MI2K and  
236 Qse2K. The LWP feedback from the adiabatic water content increase is stronger in the high-  
237 latitudes ( $5.2\% \text{ K}^{-1}$ ) than in the mid-latitudes ( $1.6\% \text{ K}^{-1}$ ), as one would expect from the nonlinear  
238 temperature-dependence of the Clausius-Clapeyron relation.

239 Within the combined microphysical component, the BF process (BF2K) is responsible for most  
240 of the LWP increase, with a smaller contribution from melting (ME2K) present only in the mid-  
241 latitudes (Fig. 3b), and homogeneous freezing and phase partitioning producing negligible results.  
242 The BF effect is realized through the temperature-dependence of the conversion rate, as opposed to  
243 the temperature threshold at which the BF process takes control. LWP increases as the BF process  
244 slows down, converting less liquid to ice. The melting of snow to rain dominates the melting of ice  
245 to rain in terms of their effects in enhancing LWP. As discussed later, this can be conceptualized as  
246 a consequence of weaker riming since there is less snow (falling ice) to collect cloud liquid. Thus,  
247 we conclude that the increase in LWP with warming results primarily from a significant weakening  
248 of the BF process.

249 The IWP feedback is more nuanced. As shown in Fig. 3c, Qse2K and MI2K produce opposite  
250 effects: IWP increases at all latitudes in the former, while it decreases in the mid-latitudes with no  
251 significant change in the high-latitudes in the latter. In Qse2K, the normalized fractional increase  
252 in the high-latitude IWP ( $7.9\% \text{ K}^{-1}$ ) is greater than the mid-latitude counterpart ( $6.7\% \text{ K}^{-1}$ ),

253 consistent with the adiabatic water content increasing with temperature at a faster rate at colder  
254 temperatures. The net result in Tse2K, to which Qse2K and MI2K add effectively linearly, is an  
255 increase in IWP, principally poleward of 45°. The relative importance of the BF process versus  
256 melting is reverse to the LWP feedback. The microphysical effect is dominated by ME2K (Fig. 3d);  
257 the enhanced melting of snow contributes to the lowering of IWP more than that of cloud ice. By  
258 contrast, BF2K gives rise to very little change in IWP. The fact that a weakening of the BF process  
259 causes a large increase in LWP, but no concurrent decrease in IWP is somewhat counter-intuitive,  
260 a point to which we will return later. (As with LWP, perturbing homogeneous freezing or phase  
261 partitioning produces no significant change in IWP.)

262 Fig. 4 shows the vertical structures of the changes in the mixing ratios of cloud liquid and ice.  
263 To better understand the underlying physical mechanisms, the main tendency terms driving the  
264 steady-state cloud liquid and ice are plotted in Figs. 5 and 6, respectively. No appreciable change  
265 in  $q_l$  is present below the freezing line in any experiment (Fig. 4) even when there are large local  
266 changes in cloud liquid tendencies, as is the case for condensation in Qse2K (Fig. 5a). It is also clear  
267 from Fig. 5 that autoconversion is the principal sink of  $q_l$  or the rain-producing mechanism above  
268 0°C in Ctrl, with accretion playing a secondary role. As explained in Section 2,  $q_{crit}$  exerts a strong  
269 control over  $q_l$  when autoconversion dominates. By contrast, the BF process and riming take over  
270 in the M-P cloud temperature range (between 0° and -40°C). As the BF process is independent of  
271  $q_l$  and riming is proportional to  $q_l$ , the enhanced condensation in Qse2K has a tendency to increase  
272  $q_l$  through riming (Fig. 5q). On the ice side, faster riming acts to increase  $q_i$  (Fig. 6e). Moreover,  
273 the increased condensation leads directly to higher  $q_i$  through the BF process (Fig. 6a), which is  
274 conditionally proportional to  $q_i^{1/3}$ . The resulting higher flux of settling ice, which is formulated to  
275 be approximately proportional to  $q_i$ , tends to further accelerate riming, but lower  $q_l$ . This cancels  
276 out much of the increase in  $q_l$  caused by the increased condensation (Fig. 4a). The end result is

277 that the normalized fractional increase in the extratropical IWP ( $6.8\% \text{ K}^{-1}$ ) is much greater than  
278 the LWP counterpart ( $1.7\% \text{ K}^{-1}$ ).

279 The imposed warming to the BF process (BF2K) slows down the BF conversion from liquid to  
280 ice (Fig. 5n). Since autoconversion and accretion play limited roles in the M-P cloud regime, an  
281 acceleration of riming (Fig. 5r) is the only way to re-establish the  $q_l$  tendency balance, causing a  
282 significant increase in  $q_l$  (Fig. 4b). This re-balancing can be conceptualized as a weaker BF process  
283 producing more cloud liquid to be scavenged by falling ice through riming. Since the  $q_l$  and  $q_i$   
284 tendencies (and their changes) are of the same magnitude but opposite signs for the BF process  
285 and riming, the effect of the two processes on  $q_i$  is dictated by the balance of their  $q_l$  counterparts  
286 (Fig. 6b and f). Because the effects of  $q_i$  are of opposing sign, there is near-zero net change in  
287 cloud ice (Fig. 4f). This somewhat counterintuitive result emphasizes the need to evaluate changes  
288 in  $q_l$  and  $q_i$  based on process changes and a dynamic re-balancing of sources and sinks.

289 The melting perturbation (ME2K) is unique in the sense that the resulting changes in cloud liquid  
290 and ice are of mirror image in terms of spatial structure (Fig. 4c and g). The main reason is that the  
291 melting perturbation effects are relatively confined to a narrow domain of a few degrees above the  
292 time-averaged freezing line. The warming-induced additional melting acts to increase the flux of  
293 rain and decrease the flux of settling ice simultaneously. Both factors have implications for  $q_l$ . The  
294 former tends to accelerate accretion with an effect of decreasing the  $q_l$  tendency, while the latter  
295 acts to slow down riming which increases the  $q_l$  tendency. The simulation shows a net increase of  
296  $q_l$ , suggesting that the latter factor prevails over the former. The signs of the simulated rate changes  
297 are consistent with the expectations, and they largely balance out each other (Fig. 5k and s), with  
298 a weaker contribution from autoconversion (Fig. 5g). On the ice side, the reduced supply of ice  
299 from riming is balanced entirely by lowering  $q_i$  and thus settling (Fig. 6g and k). The role of the

300 BF process here is negligible as it is relatively ineffective at temperatures within a few degrees of  
301 0 °C.

302 This process-level analysis illustrates why the principal components of the full warming (Tse2K)  
303 simulation, namely Qse2K, BF2K, and ME2K, increase  $q_l$  and hence LWP, as summarized schemat-  
304 ically in Fig. 7. Although they all point in the same direction, the microphysical warming com-  
305 ponents (BF2K and ME2K) are a stronger contribution to the LWP feedback than the macro-  
306 physical/thermodynamic component (Qse2K). The extratropical IWP feedback stems from a broad  
307 increase in  $q_i$  from Qse2K being offset partially by a decrease near the freezing line from ME2K.  
308 The results underscore that multiple processes with distinct characteristics are influential in shaping  
309 the LWP and IWP responses, and contradict the common picture suggested in M-P cloud feedback  
310 literature of a trade-off between ice and liquid. Here, the dominant processes which increase  
311 LWP with warming in M-P clouds are not doing so at the expense of ice, so the actual picture  
312 is more complicated than a direct conversion from ice to liquid with warming. Liquid and ice  
313 in mixed-phase clouds are not in a static equilibrium; rather, they exist in a dynamic balance of  
314 sources and sinks. These source and sink processes are directly changed by warming as opposed  
315 to a simple temperature-dependent phase partitioning.

### 316 *b. Perturbed Parameter Experiments*

317 To further explore the sensitivity of the LWP and IWP feedbacks, a set of alternative control  
318 states were created by altering three key aspects of the cloud scheme, namely the value of  $RH_c$ ,  
319 the strength of the BF process and the fall speed of ice ( $v_{fall}$ , Eqn. A7), summarized in Table  
320 1. As shown in Fig. 8, the first two changes produce a wide range of the climatological LWP  
321 (approximately a factor of 2), but little variation in IWP. Lower  $RH_c$  or weaker BF process leads to  
322 higher LWP. While exploring the insensitivity of IWP to  $RH_c$  or the BF process in more detail than

323 the previous section is beyond the scope of this work, the broad principle is that steady-state values  
324 are determined by a dynamic balance of continuing phase conversion, not a static equilibrium.  
325 When  $v_{fall}$  is varied, IWP varies widely (a factor of more than 3) with higher fall speed giving rise  
326 to lower IWP but with little spread in the climatological LWP.

327 All of these perturbed parameter experiments are subjected to 2-K warming in a way analogous  
328 to Tse2K. The resulting normalized LWP and IWP changes ( $\delta LWP$  and  $\delta IWP$ , respectively) are  
329 plotted against their climatological counterparts in Fig. 9. Ranging from 2.6 to 3.4  $\text{g m}^{-2} \text{K}^{-1}$ ,  
330 relative to 3.0  $\text{g m}^{-2} \text{K}^{-1}$  in Tse2K (Table 2), the LWP feedback is positively correlated with the  
331 climatological LWP (Fig. 9a). The best linear fit yields that  $\delta LWP = 0.045 LWP + 1.60$ , with an  $R^2$   
332 of 0.98. Thus, the fractional change can be written as  $\delta LWP/LWP = 0.045 + 1.60/LWP$ , suggesting  
333 that the marginal gain decreases with increasing LWP. Since the four experiments targeting the BF  
334 process, namely {quar, halv, doub, quad}BF, effectively demonstrate the basic behavior of the LWP  
335 feedback, we start by focusing on them in the effort to explain the latter. As shown above, the main  
336 sink terms for cloud liquid in the M-P regime are the BF process and riming. As the BF process  
337 becomes stronger from quarBF to quadBF, riming has to weaken if the total sink is constant, giving  
338 rise to lower climatological LWP, in line with the model simulations. Recall that the riming rate  
339 is proportional to cloud liquid. The process-level experiments suggest that the warming effect is  
340 realized mostly through the BF process. In these experiments, the warming-induced perturbation  
341 to the BF process is roughly proportional to its baseline rate (not shown). Therefore, the lower  
342 the climatological LWP is, the stronger the baseline BF rate and associated perturbation are. The  
343 combination translates into higher fractional change in LWP with lower climatological LWP (from  
344 a stronger BF process).

345 Lowering  $RH_c$  tends to increase LWP by enhancing condensation in a way similar to Qse2K.  
346 They differ in that the former causes a large increase in autoconversion, but without any substantial

347 change in accretion or riming, while all three processes increase in the latter. As explained before,  
348 autoconversion can adjust to forced changes such as those resulting from warming without perturb-  
349 ing cloud liquid. As a result, a control state with enhanced autoconversion should be less sensitive  
350 to warming. This explains why lowering  $RH_c$  gives rise to larger LWP, but smaller fractional in-  
351 creases in response to warming. Of interest is the minimal effect on the extratropical climatological  
352 LWP and  $\delta$ LWP from drastically changing the climatological IWP (or susceptible ice) in the ice  
353 fall speed experiments. Clearly, the LWP feedback is correlated with the climatological LWP, but  
354 not the climatological IWP. The preceding analysis also holds when the LWP feedback is further  
355 divided into the mid- and high-latitude components (not shown).

356 The IWP feedback is correlated strongly with the climatological IWP (Fig. 9b). Note that the  
357 variation in the IWP feedback is almost exclusively from the ice fall speed experiments (ranging  
358 from 0.57 to 1.70 g m<sup>-2</sup> K<sup>-1</sup>). An inspection of the best linear fit result ( $\delta$ IWP = 0.023·LWP  
359 + 0.031, with an  $R^2$  of 1.00) indicates that the intercept is so small that the warming-induced  
360 change in IWP is effectively proportional to the climatological IWP. In other words, the normalized  
361 fractional change is constant at 2.3% K<sup>-1</sup>. This relatively simple relation reflects the fact that  
362 gravitational settling is the main process through which cloud ice can be adjusted to re-establish  
363 the mass balance. As seen both from the process-level experiments and the BF-series parameter  
364 perturbation experiments, the amount of cloud ice is not sensitive to the BF process. In the  
365 meantime, riming is under the strong control of the cloud liquid balance. This leaves gravitational  
366 settling as the only way to alter cloud ice without affecting other processes substantially. Note that  
367 similar linear relationships hold if the climatological LWP and IWP are computed only for the M-P  
368 temperature range (between 0 and -40°C), confirming the independence of the LWP feedback from  
369 the climatological IWP (or susceptible ice).

## 370 4. Discussion

371 As noted in the introduction, much of the existing literature on the extratropical M-P cloud  
372 feedback centers on the correlation between the climatological SLF/T5050 and LWP feedback.  
373 Specifically, the lower SLF is or the higher T5050 is, the stronger the LWP feedback is (Tan  
374 et al. 2016; Frey and Kay 2018; McCoy et al. 2018). The presumption is that the phase change  
375 mechanism plays a crucial role, meaning that ice would melt into liquid as isotherms shift with  
376 warming. Thus, the climatological susceptible ice or IWP is thought to be predictive of the feedback  
377 strength, forming the basis of potential emergent constraints (Tan et al. 2016). A related argument  
378 is that the phase change would give rise to a decrease in precipitation efficiency (PE) and a net  
379 increase in total water path (TWP, the sum of LWP and IWP) as liquid is less efficient than ice in  
380 forming precipitation (McCoy et al. 2018). While it is clear from the previous section that the M-P  
381 cloud feedback is much more complicated than simple phase change, we further test the validity of  
382 both claims—SLF/T5050 as a predictor and decreased PE increasing TWP—against our results.

383 The climatological T5050 in the perturbed parameter experiments spans a wide range ( $\sim 15$  K)  
384 (Fig. 10). Stronger BF process and higher  $RH_c$  favor lower LWP (or SLF) and higher T5050,  
385 consistent with previous studies (e.g. Tan et al. 2016; Frey and Kay 2018). The normalized  $\delta LWP$ ,  
386 however, is strongly anti-correlated with T5050 ( $R^2 = 0.92$ , Fig. 10) as it is positively correlated  
387 with the climatological LWP (Fig. 9a). The T5050/ $\delta LWP$  anti-correlation is opposite to that  
388 expected if susceptible ice drove the LWP feedback and is contrary to the findings of Tan et al.  
389 (2016) and Frey and Kay (2018) based on the CAM5 model and of McCoy et al. (2018) based on  
390 CMIP5 models. Furthermore, as shown in Fig. 8, the climatological IWP is effectively constant for  
391 these experiments. This calls into question the hypothesis that susceptible ice controls the strength  
392 of the LWP feedback. As another evidence against the hypothesis, if the  $v_{fall}$  perturbations are

393 included, the predictive power of T5050 is significantly diminished ( $R^2 = 0.76$ , Fig. 10). The large  
394 variations in the climatological IWP, which drive the spread in T5050 in the  $v_{fall}$  perturbations, do  
395 not affect  $\delta$ LWP significantly. Thus, any connection here between T5050 and the LWP feedback is  
396 not derived from the climatological ice but rather the climatological liquid.

397 By comparing the aquaplanet versions of CAM5 and AM2.1, the latter of which uses virtually  
398 the same large-scale cloud parameterizations as our idealized model, Ceppi et al. (2016) provides  
399 important clues as how to reconcile this work with others. Note that the AM2.1 results documented  
400 in Ceppi et al. (2016) are in excellent agreement with ours despite numerous differences in model  
401 setup and experimental design, a testament to the central role of cloud parameterizations in deter-  
402 mining the feedback. Whereas both CAM5 and AM2.1 yield higher LWP in response to warming,  
403 their IWP changes differ in sign (see their Figure 2). IWP decreases in CAM5, but increases in  
404 AM2.1. Moreover, microphysical processes, especially the BF process, are responsible for the  
405 majority of the LWP increases, but cannot even account for the signs of the combined extratropical  
406 IWP changes (their Figure 7): the microphysically-induced IWP change is an increase in CAM5 and  
407 a decrease in AM2.1. Note that CAM5 implements the Morrison-Gottelman microphysics scheme  
408 (Morrison and Gottelman 2008), which differs significantly from the Rotstayn-Klein microphysics  
409 scheme (Rotstayn 1997) used in AM2.1 and our model, particularly in the treatment of ice and  
410 snow. In this sense, it is not inconceivable to see microphysically-induced IWP changes being  
411 qualitatively different between the two models. More interestingly, if one assumes linear additivity,  
412 which appears to hold, the non-microphysical component of the IWP change would be a net loss in  
413 CAM5 and a net gain in AM2.1. Our results demonstrate that the non-microphysical enhancement  
414 of IWP in AM2.1 is attributable to the adiabatic cloud water content increase, a possibility noted  
415 in Ceppi et al. (2016), raising the intriguing question of what factors can possibly overcome the  
416 rather powerful adiabatic cloud water content effect and cause the net loss seen in CAM5. There

417 are no obvious candidates at least to us. Nonetheless, it is plausible that the considerable loss of  
418 cloud ice in the warming experiments conducted with CAM5 in Tan et al. (2016) and Frey and Kay  
419 (2018) is not microphysical in origin, and thus should not be interpreted as being related to the  
420 concurrent increase of cloud liquid, which roots in microphysics. This mechanistic understanding  
421 casts further doubt on the susceptible ice hypothesis and other related arguments. From a broader  
422 perspective, Ceppi et al. (2016) also noted a robust extratropical LWP increase with warming in  
423 the CMIP5 model ensemble mean, without a compensating large decrease in IWP. This is consis-  
424 tent with other studies showing diverse extratropical LWP and IWP feedbacks in models beyond  
425 the two highlighted by Ceppi et al. (2016). For example, Lohmann and Neubauer (2018), using  
426 ECHAM6-HAM2 with microphysics after Lohmann and Roeckner (1996), found no increase in  
427 ECS with increased SLF. McCoy et al. (2021) showed that among CMIP5 and CMIP6 GCMs,  
428 most show an increase in liquid along with a slight reduction in ice.

429 To quantify whether changes in PE affect total cloud water, we calculate the large-scale PE  
430 as defined in Zhao (2014), which is the ratio of the total cloud condensation rate (the sum of  
431 condensation and deposition fluxes) to surface precipitation and represents the fraction of the  
432 condensate that subsequently rains out. There is a slight increase in PE with warming (80.5% in  
433 Ctrl versus 81.1% in Tse2K). This results from microphysical increases (80.7% in BF2K and 80.8%  
434 in ME2K) being offset by a macrophysical decrease (80.0% in Qse2K). Another measure of a PE  
435 effect is surface precipitation normalized by TWP ( $P/TWP$ ) as in McCoy et al. (2015), which can  
436 be thought of as the inverse of the cloud water residence time. Following the Clausius-Clapeyron  
437 relation, the extratropical surface precipitation increases by  $6.9\% K^{-1}$  in Tse2K and Qse2K, but  
438 remains essentially constant in the microphysical experiments.  $P/TWP$  increases by 1.9% from  
439  $1.03 \text{ hr}^{-1}$  in Ctrl to  $1.05 \text{ hr}^{-1}$  in Tse2K. Again, the net result is a slight decrease in the cloud water  
440 residence time or a slight increase in PE. These results do not support a PE effect with warming

441 here as widely claimed (e.g., at the heart of the argument of Bjordal et al. 2020). In our model, the  
442 weakening of the BF process (BF2K) increases TWP while keeping precipitation nearly constant,  
443 suggesting that the BF process alone could affect PE, and thus should be the focus of research to  
444 improve its representation in models.

445 In the absence of PE-mediated strong phase change effect, the adiabatic cloud water content  
446 effect is shown to be responsible for increasing TWP by enhancing both liquid and ice. McCoy  
447 et al. (2015) observed that increasing TWP was a significant contribution to increased extratropical  
448 LWP in CMIP5 models, with only 20–80% of the LWP increase being due to phase re-partitioning.  
449 Using observations and modeling, McCoy et al. (2019) highlighted the primacy of the adiabatic  
450 cloud water content effect in explaining the increase in LWP with warming in extratropical cy-  
451 clones. It was found that more than 80% of the enhanced Southern Ocean extratropical cyclone  
452 LWP in GCMs from warming can be predicted based on the relationship between the climatological  
453 warm conveyor belt moisture flux and cyclone LWP and the change in moisture flux with warming  
454 (see also McCoy et al. 2020). While phase change may play a role in the remaining unexplained  
455 LWP increases, especially in the poleward half of cyclones, it is clearly a secondary mechanism.  
456 A ground-based observational study (Terai et al. 2019) found that both the moist adiabatic scaling  
457 and phase partitioning are equally important for explaining the increase in LWP with warming at  
458 cold temperatures. A complementary space-based observational study (Tan et al. 2019), however,  
459 suggests phase change is more important than the adiabatic cloud water content increase in ex-  
460 plaining the increase in cloud optical depth with cloud top temperature. More research is clearly  
461 needed for elucidating the relative importance of the two mechanisms.

## 462 **5. Conclusions**

463 This study used an idealized GCM to perform a set of process-level experiments which delineated  
464 three key mechanisms of the extratropical LWP feedback involving M-P clouds: higher adiabatic  
465 cloud water content, weaker liquid-to-ice conversion through the BF process, and strengthened  
466 melting of ice and snow to rain with associated impacts on riming. Over half of the extratropical  
467 LWP increase can be attributed to the weakening of the BF process, without a corresponding  
468 decrease in IWP. The extratropical IWP in fact increases with warming due to the adiabatic cloud  
469 water effect, with a small offset caused by stronger melting. Warming experiments in a perturbed  
470 parameter ensemble demonstrate a strong dependence of the LWP feedback on the climatological  
471 LWP and independence from the climatological IWP. T5050 is anti-correlated with  $\delta\text{LWP}$  and is  
472 therefore only useful as a predictor insofar as it represents the climatological LWP as opposed to  
473 the climatological IWP. No associated decrease in PE is found.

474 The overarching goal of this study is to improve mechanistic understanding of the extratropical  
475 M-P cloud feedback. Our results help refine the current physical conceptualization of the LWP  
476 feedback as more nuanced than simple phase change, involving impacts of higher adiabatic cloud  
477 water content, weaker cloud liquid sinks such as the BF process, and indirect phase changes  
478 moderated by precipitation processes (especially riming). Liquid and ice in M-P clouds are  
479 in a dynamic equilibrium with microphysical process efficiencies defining time-averaged phase  
480 partitioning and its change with warming. These results are helpful for guiding efforts to constrain  
481 M-P parameterizations in GCMs through process-oriented diagnostics. In particular, the effect of  
482 warming on the BF process, which is at the heart of M-P cloud microphysics, should be better  
483 understood and represented in GCMs. In addition to the BF process, the climatological LWP  
484 needs to be better constrained. Not only is it shown here to be predictive of the LWP feedback, but

485 also the radiative impact of increases in LWP is highly dependent on the control state (Bodas-  
486 Salcedo et al. 2016, 2019). Finally, similar process-based studies, especially among varying  
487 microphysics schemes, are vital, as cloud water source and sink efficiencies define the M-P cloud  
488 phase partitioning (Ceppi et al. 2016). M-P cloud studies should show results at the process level  
489 to better conclude as to the driving mechanisms and implications for ECS. Because of the need  
490 for re-tuning of complex GCMs to restore radiative balance when M-P physics are perturbed (as  
491 in Tan et al. 2016; Frey and Kay 2018), idealized setups such as that utilized here present a clean,  
492 complementary approach for elucidating causal relationships.

493 *Acknowledgments.* The authors acknowledge Nadir Jeevanjee and David Paynter for helpful feed-  
494 back and Daniel McCoy for useful discussion. M.E.F. was supported by award NA18OAR4320123  
495 from the National Oceanic and Atmospheric Administration, U.S. Department of Commerce, and  
496 award AWD1005319 from the National Science Foundation.

497 *Data availability statement.* The output from the simulations described in this manuscript is  
498 archived at the Geophysical Fluid Dynamics Laboratory and is available upon request.

## 499 APPENDIX

### 500 **Microphysical Transformation Equations**

501 The following equations are those parameterized in the microphysical scheme used herein (after  
502 Rotstayn 1997; Rotstayn et al. 2000).

503 *a. Precipitation Formation Processes*

504 *Autoconversion*: the time rate change of grid mean liquid from autoconversion is parameterized

505 as:

$$\frac{\partial q_l}{\partial t} \Big|_{au} = -q_a \times \left( \frac{0.104 g \rho^{4/3} E_{c,au}}{\mu (N \rho_l)^{1/3}} \right) \times (q_l/q_a)^{7/3} \times H(r_d - r_d^{au}) \quad (A1)$$

506 where  $\mu$  is the dynamic viscosity of air,  $E_{c,au}$  is the mean collection efficiency of the autoconversion

507 process,  $\rho_l$  is the density of pure liquid, and  $N$  is the number of cloud droplets per unit volume. In

508 the Heaviside function,  $H$ ,  $r_d^{au}$  is a critical drop radius that the mean volume radius of cloud drops,

509  $r_d$ , must exceed for autoconversion to occur, where:

$$\rho q_l / q_a = 4\pi N \rho_l r_d^3 / 3 \quad (A2)$$

510 Autoconversion is limited to that which would decrease  $q_l$  to the threshold:

$$MAX \left( - \frac{\partial q_l}{\partial t} \Big|_{au} \right) = \ln \left( \frac{\rho q_l / q_a}{4\pi N \rho_l (r_d^{au})^3 / 3} \right) \times \frac{q_l}{\Delta t_{cld}} \quad (A3)$$

511 *Accretion*: the time rate change of grid mean liquid from accretion is parameterized as:

$$\frac{\partial q_l}{\partial t} \Big|_{acc} = -a_{rain}^{cld} \times 65.8 E_{c,acc} (R_{rain}^{cld} / \rho_l a_{rain}^{cld})^{7/9} \times (q_l / q_a) \quad (A4)$$

512 where  $R_{rain}^{cld}$  is the grid mean flux of rain entering the rid box from above that enters saturated air,

513  $a_{rain}^{cld}$  is the portion of the grid box that this occurs in, and  $E_{c,acc}$  is the collection efficiency between

514 rain drops and cloud droplets which is parameterized as:

$$E_{c,acc} = r_d^2 / (r_d^2 + 20.5 \mu^2) \quad (A5)$$

515 *Gravitational Settling*: the sink of cloud ice due to gravitation settling is:

$$\frac{\partial q_i}{\partial t} \Big|_{gr} = - \frac{\partial}{\partial p} \{ q_a \times \rho g V_f \times (q_i / q_a) \} \quad (A6)$$

516 where  $V_f$  is the fall speed the cloud ice fall as relative to the large-scale vertical motion and is  
 517 parameterized as:

$$V_f = 3.29(\rho q_i/q_a)^{0.16} \quad (\text{A7})$$

518 *b. Conversions between Liquid and Ice:*

519 *BF Process:* the time rate change of the Bergeron-Findeisen process (growth of an ice crystal  
 520 from preferential condensation) is parameterized as:

$$\left. \frac{\partial q_l}{\partial t} \right|_{\text{berg}} = - \frac{q_a \times (N_i/\rho)^{2/3} \times 7.8 \times (\text{MAX}(q_i/q_a, M_{i0}N_i/\rho))^{1/3}}{(\rho_i)^{2/3} \times (A + B)} \quad (\text{A8})$$

521 where  $N_i$  is the number of ice nuclei per unit volume,  $M_{i0}$  is the mass ( $10^{-12}$ ) of an initial  
 522 crystal assumed to always be present,  $\rho_i$  is the mass density of pristine ice crystals. Additionally,  
 523  $A = (L_v/K_a T) \cdot ((L_v/R_v T) - 1)$  and  $B = R_v T / \chi e_s$ , where  $K_a$  is the thermal conductivity of air,  $\chi$   
 524 is the diffusivity of water vapor in air, and  $R_v$  is the gas constant for water vapor. The ice nuclei  
 525 density,  $N_i$ , is parameterized assuming the air is a liquid water saturation:

$$N_i = 1000 \exp \left[ 12.96 \frac{(e_{sl} - e_{si})}{e_{si}} - 0.639 \right] \quad (\text{A9})$$

526 where  $e_{sl}$  and  $e_{si}$  are the saturation vapor pressures over liquid and ice, respectively.

527 *Riming:* the time rate change of riming (falling ice colliding and coalescing with cloud droplets)  
 528 is parameterized as:

$$\left. \frac{\partial q_l}{\partial t} \right|_{\text{rim}} = -a_{\text{snow}}^{\text{cld}} \times \lambda_f E_{c,\text{rim}} (R_{\text{snow}}^{\text{cld}} / 2\rho_i a_{\text{snow}}^{\text{cld}}) \times (q_l/q_a) \quad (\text{A10})$$

529 where  $\rho_i$  is the assumed density of falling ice crystals,  $R_{\text{snow}}^{\text{cld}}$  is the grid mean flux of settling ice  
 530 entering the rid box from above that enters saturated air,  $a_{\text{snow}}^{\text{cld}}$  is the portion of the grid box that this  
 531 occurs in,  $E_{c,\text{rim}}$  is the collection efficiency for the riming process (fixed), and  $\lambda_f$  is parameterized  
 532 as a function of temperature:

$$\lambda_f = 1.6 \times 10^3 \cdot 10^{0.023(276.16K - T)} \quad (\text{A11})$$

## 533 **References**

- 534 Betts, A. K., and Harshvardhan, 1987: Thermodynamic constraint on the cloud liquid water  
535 feedback in climate models. *J. Geophys. Res.*, **92**, 8483–8485, doi:10.1029/JD092iD07p08483.
- 536 Bjordal, J., T. Storelvmo, K. Alterskjær, and T. Carlsen, 2020: Equilibrium climate sensitivity  
537 above 5°C plausible due to state-dependent cloud feedback. *Nat. Geosci.*, **23**, 718–721, doi:  
538 10.1038/s41561-020-00649-1.
- 539 Bodas-Salcedo, A., P. G. Hill, K. Furtado, K. D. Williams, P. R. Field, J. C. Manners, P. Hyder,  
540 and S. Kato, 2016: Large contribution of supercooled liquid clouds to the solar radiation budget  
541 of the Southern Ocean. *J. Climate*, **29**, 4213–4228, doi:10.1175/JCLI-D-15-0564.1.
- 542 Bodas-Salcedo, A., J. P. Mulcahy, T. Andrews, K. D. Williams, M. A. Ringer, P. R. Field, and G. S.  
543 Elsaesser, 2019: Strong dependence of atmospheric feedbacks on mixed-phase microphysics  
544 and aerosol-cloud interactions in HadGEM3. *J. Adv. Model. Earth Syst.*, **11**, 1735–1758, doi:  
545 10.1029/2019MS001688.
- 546 Ceppi, P., F. Brient, M. D. Zelinka, and D. L. Hartmann, 2017: Cloud feedback mechanisms and  
547 their representation in global climate models. *WIREs Clim. Change*, **8**, doi:10.1002/wcc.465.
- 548 Ceppi, P., and D. L. Hartmann, 2015: Connections between clouds, radiation, and midlatitude  
549 dynamics: A review. *Curr. Clim. Change. Rep.*, **1**, 94–102, doi:10.1007/s40641-015-0010-x.
- 550 Ceppi, P., D. L. Hartmann, and M. J. Webb, 2016: Mechanisms of the negative shortwave cloud  
551 feedback in middle to high latitudes. *J. Climate*, **29**, 139–157, doi:10.1175/JCLI-D-15-0327.1.
- 552 Cesana, G., and T. Storelvmo, 2017: Improving climate projections by understanding how cloud  
553 phase affects radiation. *J. Geophys. Res. Atmos.*, **122**, 4594–4599, doi:10.1002/2017JD026927.

554 Cesana, G., D. E. Waliser, X. Jiang, and J. F. Li, 2015: Multimodel evaluation of cloud phase  
555 transition using satellite and reanalysis data. *J. Geophys. Res. Atmos.*, **120**, 7871–7892, doi:  
556 10.1002/2014JD022932.

557 Frey, W. R., and J. E. Kay, 2018: The influence of extratropical cloud phase and amount feedbacks  
558 on climate sensitivity. *Climate Dyn.*, **50**, 3097–3116, doi:10.1007/s00382-017-3796-5.

559 Galewsky, J., A. Sobel, and I. M. Held, 2005: Diagnosis of subtropical humidity dynamics using  
560 tracers of last saturation. *J. Atmos. Sci.*, **62**, 3353–3367, doi:10.1175/JAS3533.1.

561 Gettelman, A., and S. C. Sherwood, 2016: Processes responsible for cloud feedback. *Curr. Clim.*  
562 *Change Rep.*, **2**, 179–189, doi:10.1007/s40641-016-0052-8.

563 Golaz, J. C., M. Salzmann, L. J. Donner, L. W. Horowitz, Y. Ming, and M. Zhao, 2011:  
564 Sensitivity of the aerosol indirect effect to subgrid variability in the cloud parameterization  
565 of the GFDL atmosphere general circulation model AM3. *J. Climate*, **24**, 3145–3160, doi:  
566 10.1175/2010JCLI3945.1.

567 Gordon, N. D., and S. A. Klein, 2014: Low-cloud optical depth feedback in climate models. *J.*  
568 *Geophys. Res. Atmos.*, **119**, 6052–6065, doi:10.1002/2013JD021052.

569 Held, I. M., 2005: The gap between simulation and understanding in climate modeling. *Bull. Amer.*  
570 *Meteor. Soc.*, **86**, 1609–1614, doi:10.1175/BAMS-86-11-1609.

571 Held, I. M., 2014: Simplicity amid complexity. *Science*, **343**, 1206–1207, doi:10.1126/science.  
572 1248447.

573 Held, I. M., and M. J. Suarez, 1994: A proposal for the intercomparison of the dynamical  
574 cores of atmospheric general circulation models. *Bull. Amer. Meteor. Soc.*, **75**, 1825–1830,  
575 doi:10.1175/1520-0477(1994)075<1825:APFTIO>2.0.CO;2.

- 576 Klein, S. A., and Coauthors, 2009: Intercomparison of model simulations of mixed-phase clouds  
577 observed during the ARM Mixed-Phase Arctic Cloud Experiment. I: Single-layer cloud. *Quart.*  
578 *J. Roy. Meteor. Soc.*, **135**, 979–1002, doi:10.1002/qj.416.
- 579 Korolev, A., and Coauthors, 2017: Mixed-phase clouds: Progress and challenges. *Meteor. Monogr.*,  
580 **58**, 5.1–5.50, doi:10.1175/AMSMONOGRAPHSâĀĀDâĀĀ17âĀĀ0001.1.
- 581 Lohmann, U., and D. Neubauer, 2018: The importance of mixed-phase and ice clouds for climate  
582 sensitivity in the global aerosol–climate model ECHAM6-HAM2. *Atmos. Chem. Phys.*, **18**,  
583 8807–8828, doi:10.5194/acp-18-8807-2018.
- 584 Lohmann, U., and E. Roeckner, 1996: Design and performance of a new cloud microphysics  
585 scheme developed for the ECHAM general circulation model. *Climate Dyn.*, **12**, 557–572,  
586 doi:10.1007/BF00207939.
- 587 McCoy, D. T., P. Field, A. Bodas-Salcedo, G. S. Elsaesser, and M. D. Zelinka, 2020: A regime-  
588 oriented approach to observationally constraining extratropical shortwave cloud feedbacks. *J.*  
589 *Climate*, **33**, 9967–9983, doi:10.1175/JCLI-D-19-0987.1.
- 590 McCoy, D. T., M. E. Frazer, P. Field, M. D. Zelinka, G. S. Elsaesser, J. Muelmenstaedt, I. Tan, and  
591 Z. J. Lebo, 2021: Constraints on changes in the extratropical storm track predict high climate  
592 sensitivity. *in prep.*
- 593 McCoy, D. T., D. L. Hartmann, and D. P. Grosvenor, 2014: Observed Southern Ocean cloud prop-  
594 erties and shortwave reflection. Part I: Calculation of SW flux from observed cloud properties.  
595 *J. Climate*, **27**, 8836–8857, doi:10.1175/JCLI-D-14-00287.1.

596 McCoy, D. T., D. L. Hartmann, and M. D. Zelinka, 2018: Mixed-phase cloud feedbacks. *Mixed-*  
597 *Phase Clouds: Observations and Modeling*, C. Andronache, Ed., Elsevier, 215–236, doi:10.  
598 1016/B978-0-12-810549-8.00009-X.

599 McCoy, D. T., D. L. Hartmann, M. D. Zelinka, P. Ceppi, and D. P. Grosvenor, 2015: Mixed-phase  
600 cloud physics and Southern Ocean cloud feedback in climate models. *J. Geophys. Res. Atmos.*,  
601 **120**, 9539–9554, doi:10.1002/2015JD023603.

602 McCoy, D. T., I. Tan, D. L. Hartmann, M. D. Zelinka, and T. Storelvmo, 2016: On the relationships  
603 among cloud cover, mixed-phase partitioning, and planetary albedo in GCMs. *J. Adv. Model.*  
604 *Earth Syst.*, **8**, 650–668, doi:10.1002/2015MS000589.

605 McCoy, D. T., and Coauthors, 2019: Cloud feedbacks in extratropical cyclones: insight from long-  
606 term satellite data and high-resolution global simulations. *Atmos. Chem. Phys.*, **19**, 1147–1172,  
607 doi:10.5194/acp-19-1147-2019.

608 Ming, Y., and I. M. Held, 2018: Modeling water vapor and clouds as passive tracers in an idealized  
609 GCM. *J. Climate*, **31**, 775–786, doi:10.1175/JCLI-D-16-0812.1.

610 Morrison, H., G. de Boer, G. Feingold, J. Harrington, M. D. Shupe, and K. Sulia, 2011: Resilience  
611 of persistent arctic mixed-phase clouds. *Nat. Geosci.*, **5**, 11–17, doi:10.1038/ngeo1332.

612 Morrison, H., and A. Gettelman, 2008: A new two-moment bulk stratiform cloud microphysics  
613 scheme in the Community Atmosphere Model, version 3 (CAM3). Part I: Description and  
614 numerical tests. *J. Climate*, **21**, 3642–3659, doi:10.1175/2008JCLI2105.1.

615 Pierrehumbert, R. T., H. Brogniez, and R. Roca, 2007: On the relative humidity of the atmosphere.  
616 *The Global Circulation of the Atmosphere*, T. Schneider, and A. H. Sobel, Eds., Princeton  
617 University Press, 143–185.

- 618 Rotstayn, L. D., 1997: A physically based scheme for the treatment of stratiform clouds and  
619 precipitation in large-scale models. I: Description and evaluation of the microphysical processes.  
620 *Q. J. R. Meteorol. Soc.*, **123**, 1227–1282.
- 621 Rotstayn, L. D., B. F. Ryan, and J. J. Katzfey, 2000: A scheme for calculation of the liquid fraction  
622 in mixed-phase clouds in large-scale models. *Mon. Wea. Rev.*, **128**, 1070–1088.
- 623 Sherwood, S. C., and Coauthors, 2020: An assessment of Earth’s climate sensitivity using multiple  
624 lines of evidence. *Reviews of Geophysics*, **58**, e2019RG000678, doi:10.1029/2019RG000678.
- 625 Soden, B. J., and G. A. Vecchi, 2011: The vertical distribution of cloud feedback in coupled  
626 ocean-atmosphere models. *Geophys. Res. Lett.*, **38**, L12704, doi:10.1029/2011GL047632.
- 627 Somerville, R. C. J., and L. A. Remer, 1984: Cloud optical thickness feedbacks in the CO<sub>2</sub> climate  
628 problems. *J. Geophys. Res. Atmos.*, **89**, 9668–9672, doi:10.1029/JD089iD06p09668.
- 629 Stephens, G. L., 1978: Radiation profiles in extended water clouds. II. Parameterization schemes.  
630 *J. Atmos. Sci.*, **35**, 2123–2132, doi:10.1175/1520-0469(1978)035<2123:RPIEWC>2.0.CO;2.
- 631 Storelvmo, T., I. Tan, and A. V. Korolev, 2015: Cloud phase changes induced by CO<sub>2</sub> warming—a  
632 powerful yet poorly constrained cloud-climate feedback. *Curr. Clim. Change Rep.*, **1**, 288–296,  
633 doi:10.1007/s40641-015-0026-2.
- 634 Tan, I., L. Oreopoulos, and N. Cho, 2019: The role of thermodynamic phase shifts in cloud  
635 optical depth variations with temperature. *Geophys. Res. Lett.*, **46**, 4502–4511, doi:10.1029/  
636 2018GL081590.
- 637 Tan, I., T. Storelvmo, and M. D. Zelinka, 2016: Observational constraints on mixed-phase clouds  
638 imply higher climate sensitivity. *Science*, **352**, 224–227, doi:10.1126/science.aad5300.

- 639 Tan, I., T. Storelvmo, and M. D. Zelinka, 2018: The climatic impact of thermodynamic phase  
640 partitioning in mixed-phase clouds. *Mixed-Phase Clouds: Observations and Modeling*, C. An-  
641 dronache, Ed., Elsevier, 237–264, doi:10.1016/B978-0-12-810549-8.00010-6.
- 642 Terai, C., R. Y. Zhang, S. A. Klein, M. D. Zelinka, J. C. Chiu, and Q. Min, 2019: Mechanisms  
643 behind the extratropical stratiform low-cloud optical depth response to temperature in ARM site  
644 observations. *J. Geophys. Res. Atmos.*, **124**, 2127–2147, doi:10.1029/2018JD029359.
- 645 Terai, C. R., S. A. Klein, and M. D. Zelinka, 2016: Constraining the low-cloud optical depth  
646 feedback at middle and high latitudes using satellite observations. *J. Geophys. Res. Atmos.*, **121**,  
647 9696–9716, doi:10.1002/2016JD025233.
- 648 Tselioudis, G. W., B. Rossow, and D. Rind, 1992: Global patterns of cloud optical thickness  
649 variation with temperature. *J. Climate*, **5**, doi:0.1175/1520-0442(1992)005<1484:GPOCOT>2.  
650 0.CO;2.
- 651 Vial, J., J.-L. Dufresne, and S. Bony, 2013: On the interpretation of inter-model spread in CMIP5  
652 climate sensitivity estimates. *Climate Dyn.*, **41**, 3339–3362, doi:10.1007/s00382-013-1725-9.
- 653 Wall, C. J., and D. L. Hartmann, 2015: On the influence of poleward jet shift on shortwave cloud  
654 feedback in global climate models. *J. Adv. Model. Earth Syst.*, **7**, doi:10.1002/2015MS000520.
- 655 Zelinka, M. D., T. A. Myers, S. P.-C. D. T. McCoy, P. M. Caldwell, P. Ceppi, S. A. Klein, and K. E.  
656 Taylor, 2020: Causes of higher climate sensitivity in CMIP6 models. *Geophys. Res. Lett.*, **47**,  
657 e2019GL085782, doi:10.1029/2019GL085782.
- 658 Zelinka, M. D., C. Zhou, and S. A. Klein, 2016: Insights from a refined decomposition of cloud  
659 feedbacks. *Geophys. Res. Lett.*, **43**, 9259–9269, doi:10.1002/2016GL069917.

660 Zhao, M., 2014: An investigation of the connections among convection, clouds, and climate  
661 sensitivity in a global climate model. *J. Climate*, **27**, 1845–1862, doi:10.1175/JCLI-D-13-00145.  
662 1.

663 **LIST OF TABLES**

664 **Table 1.** Description of the experiments. . . . . 34

665 **Table 2.** Normalized changes in LWP and IWP ( $\text{g m}^{-2} \text{K}^{-1}$ ) in the process-level exper-  
666 iments. The normalized fractional changes ( $\% \text{K}^{-1}$ ) are in parentheses. The  
667 climatological values ( $\text{g m}^{-2}$ ) in Ctrl are also given. . . . . 35

TABLE 1. Description of the experiments.

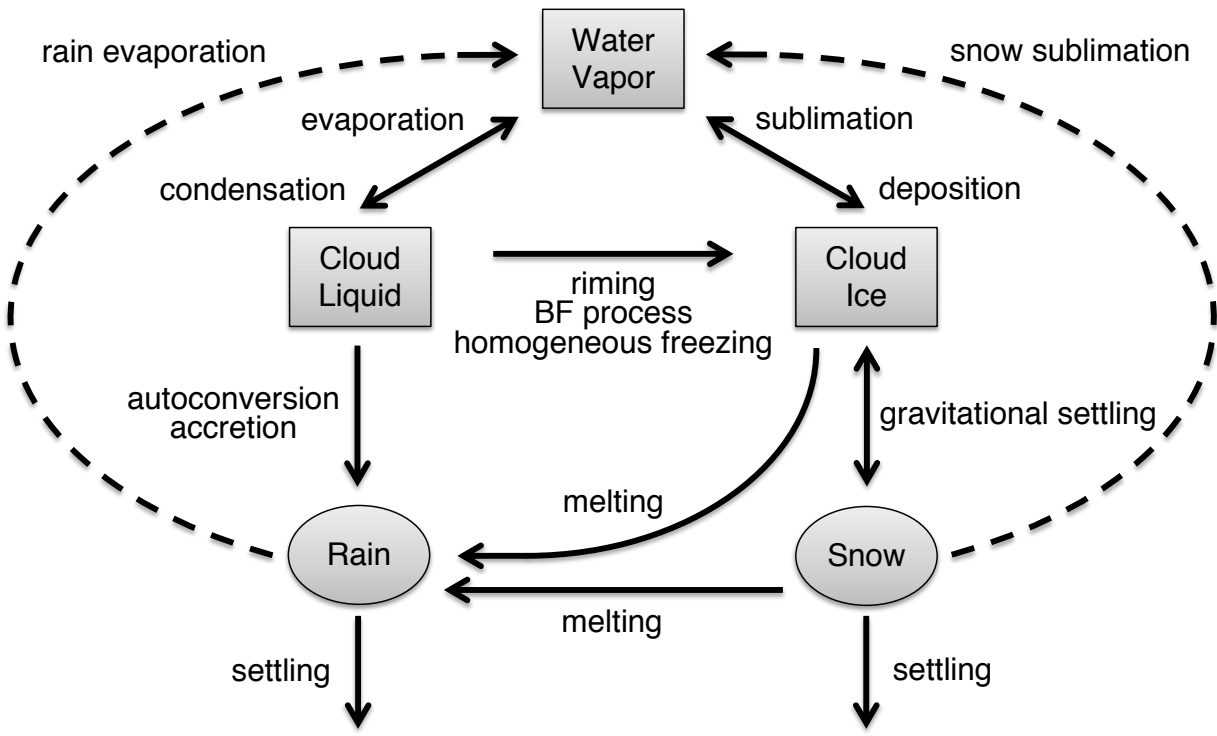
Name(s)	Perturbation(s)
Ctrl	the control with $RH_c = 83.3\%$
Tse2K	2-K warming applied to the cloud scheme and surface evaporation
Qse2K	2-K warming applied to calculation of $q_s$ for the cloud scheme and surface evaporation
MI2K	2-K warming applied to the BF process, melting, homogeneous freezing, and initial phase partitioning
BF2K	2-K warming applied to the BF process
ME2K	2-K warming applied to melting
{quar, halv, doub, quad}BF	the BF conversion rate multiplied by {0.25, 0.5, 2, 4}
rh{767, 800, 867, 900}	$RH_c = \{76.7\%, 80\%, 86.7\%, 90\%\}$
v{050, 075, 125, 150}	the ice fall speed multiplied by {0.5, 0.75, 1.25, 1.5}
{name}_Tse2K	the corresponding Tse2K experiment for {name} (e.g., quarBF_Tse2K)

668 TABLE 2. Normalized changes in LWP and IWP ( $\text{g m}^{-2} \text{K}^{-1}$ ) in the process-level experiments. The normalized  
669 fractional changes ( $\% \text{K}^{-1}$ ) are in parentheses. The climatological values ( $\text{g m}^{-2}$ ) in Ctrl are also given.

	Extratropics		Mid-Latitudes		High-Latitudes	
	LWP	IWP	LWP	IWP	LWP	IWP
Ctrl	29.9	35.6	38.3	42.7	4.6	14.1
Tse2K	3.0 (9.9)	0.9 (2.4)	3.6 (9.3)	0.8 (1.9)	1.1 (24.2)	1.0 (7.2)
Qse2K	0.5 (1.7)	2.4 (6.8)	0.6 (1.6)	2.8 (6.7)	0.2 (5.2)	1.1 (7.9)
MI2K	2.2 (7.4)	-1.4 (-4.0)	2.6 (6.9)	-1.9 (-4.4)	0.9 (19.4)	0.0 (-0.3)
BF2K	1.7 (5.5)	-0.1 (-0.2)	1.9 (5.0)	-0.1 (-0.2)	0.9 (18.7)	0.0 (0.2)
ME2K	0.6 (2.1)	-1.4 (-3.9)	0.8 (2.1)	-1.8 (-4.2)	0.0 (0.8)	-0.1 (-0.5)

## LIST OF FIGURES

670		
671	<b>Fig. 1.</b>	Schematic of tracers and processes in the cloud microphysics scheme. Quantities in rectangles are prognostic tracers, and those in ovals are diagnostic variables. . . . . 37
672		
673	<b>Fig. 2.</b>	Zonal-mean LWP and IWP ( $\text{g m}^{-2}$ ) in Ctrl and Tse2K experiments. . . . . 38
674	<b>Fig. 3.</b>	Normalized changes in the zonal-mean extratropical LWP (the upper panels) and IWP (the lower panels) ( $\text{g m}^{-2} \text{K}^{-1}$ ) in the process-level experiments. . . . . 39
675		
676	<b>Fig. 4.</b>	Vertical distributions of the normalized changes in the zonal-mean mixing ratios of cloud liquid and ice ( $10^{-6} \text{kg kg}^{-1} \text{K}^{-1}$ ) in the key process-level experiments. Differences between the perturbation and Ctrl runs are shown as colored shading. Ctrl run values are depicted by the contours with a spacing of $5 \cdot 10^{-6} \text{kg kg}^{-1}$ . Thick grey lines show the $0^\circ\text{C}$ and $-40^\circ\text{C}$ isotherms. The x- and y-axes are latitude and pressure (hPa), respectively. . . . . 40
677		
678		
679		
680		
681	<b>Fig. 5.</b>	Vertical distributions of the normalized changes in the zonal-mean time tendency terms of cloud liquid mixing ratio ( $10^{-9} \text{kg kg}^{-1} \text{s}^{-1} \text{K}^{-1}$ ) in the key process-level experiments. Differences between the perturbation and Ctrl runs are shown as colored shading where a positive value indicates an increase in cloud liquid tendency. Ctrl run values are represented by the contours with a spacing of $1 \cdot 10^{-9} \text{kg kg}^{-1} \text{s}^{-1}$ . The tendency terms shown are condensation, autoconversion, accretion, the BF process, and riming. Thick grey lines are the $0^\circ\text{C}$ and $-40^\circ\text{C}$ isotherms. The x- and y-axes are latitude and pressure (hPa), respectively. . . . . 41
682		
683		
684		
685		
686		
687		
688	<b>Fig. 6.</b>	As Fig. 5 but for cloud ice instead of cloud liquid, with tendency terms shown being the BF process, riming, and gravitational ice settling. . . . . 42
689		
690	<b>Fig. 7.</b>	Summary of the three main processes (highlighted by Qse2K, BF2K, and ME2K experiments) underlying the LWP/IWP feedback. Arrow width and direction represent the relative magnitude and sign (upward denoting an increase) of the LWP/IWP changes, respectively. . . . . 43
691		
692		
693	<b>Fig. 8.</b>	Climatological LWP ( $\text{g m}^{-2}$ ) plotted against the climatological IWP ( $\text{g m}^{-2}$ ) in the perturbed parameter experiments. . . . . 44
694		
695	<b>Fig. 9.</b>	Normalized changes in LWP/IWP ( $\text{g m}^{-2} \text{K}^{-1}$ ) in the full warming (Tse2K) experiments plotted against the climatological LWP/IWP ( $\text{g m}^{-2}$ ) in the perturbed parameter experiments. Panels (a) and (b) are for LWP and IWP, respectively. The rectangle in Panel (b) is a blowup of the data points clustered around Ctrl. . . . . 45
696		
697		
698		
699	<b>Fig. 10.</b>	Normalized changes in LWP ( $\text{g m}^{-2} \text{K}^{-1}$ ) in the full warming (Tse2K) experiments plotted against the climatological T5050. The black and orange dotted lines represent the best linear fits without and with the ice fall speed experiments, respectively. . . . . 46
700		
701		



702 FIG. 1. Schematic of tracers and processes in the cloud microphysics scheme. Quantities in rectangles are  
 703 prognostic tracers, and those in ovals are diagnostic variables.

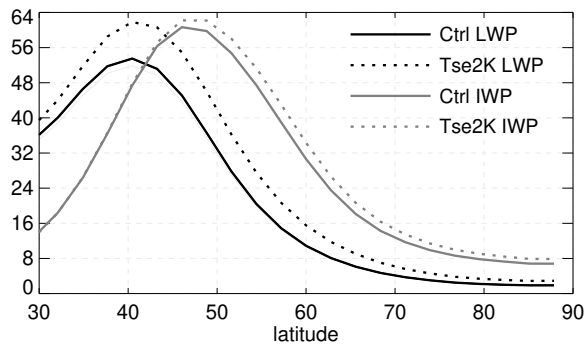
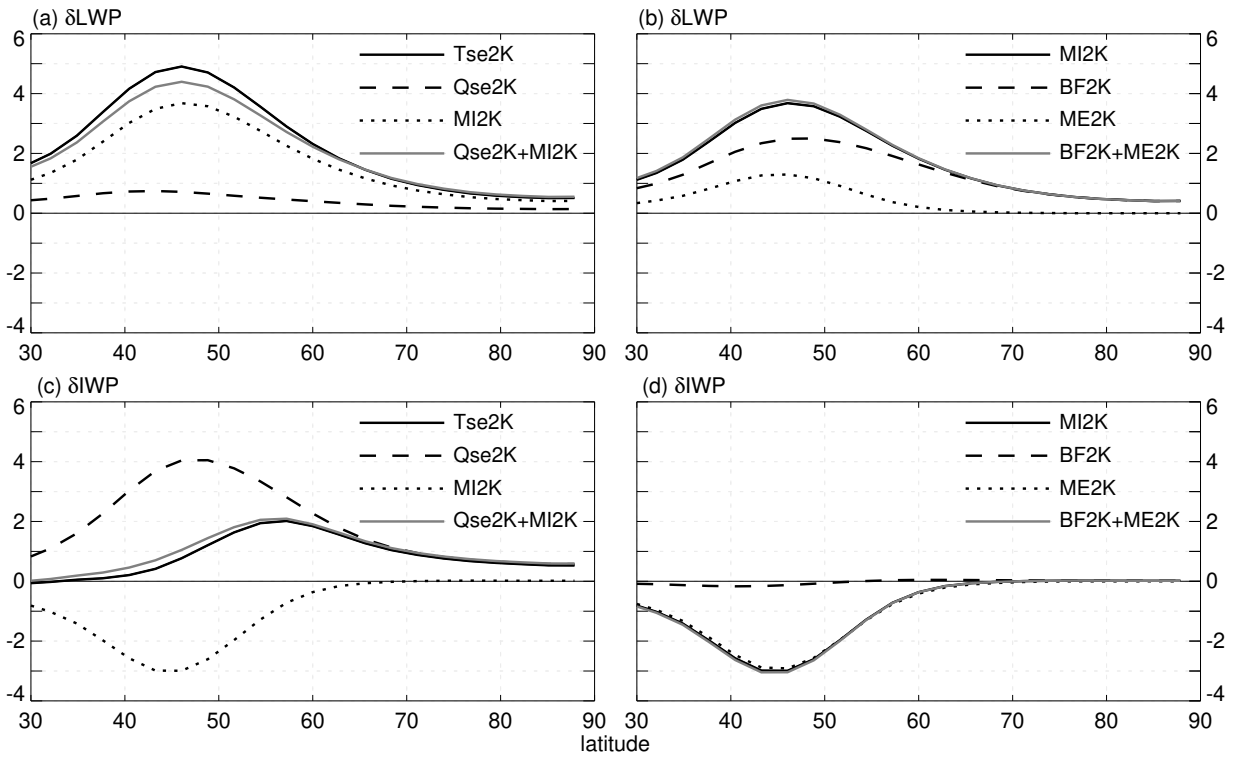
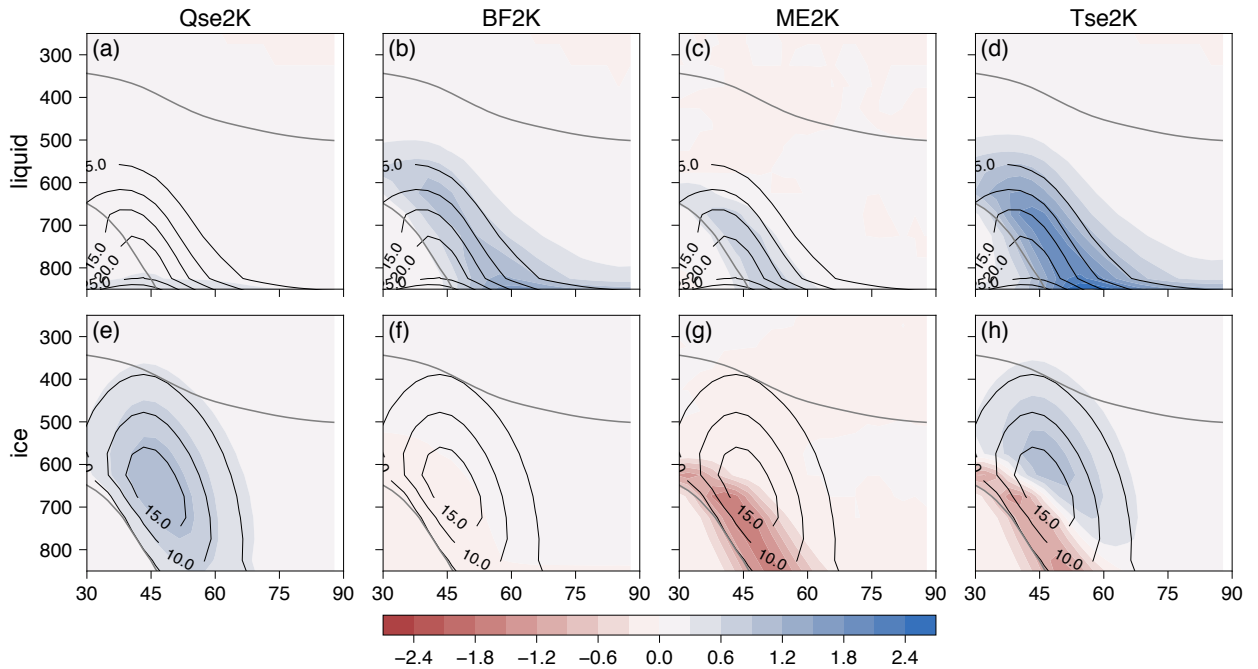


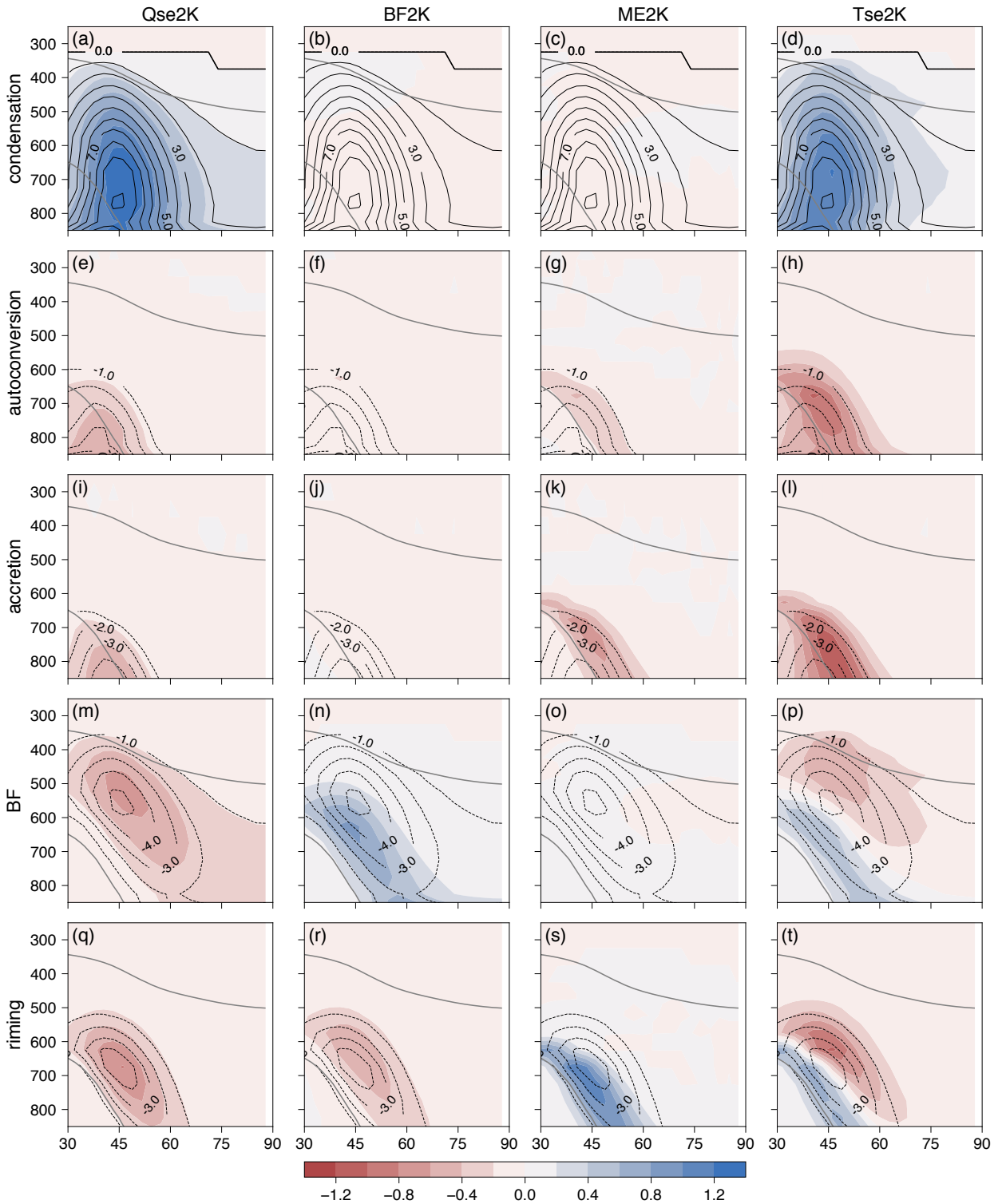
FIG. 2. Zonal-mean LWP and IWP ( $\text{g m}^{-2}$ ) in Ctrl and Tse2K experiments.



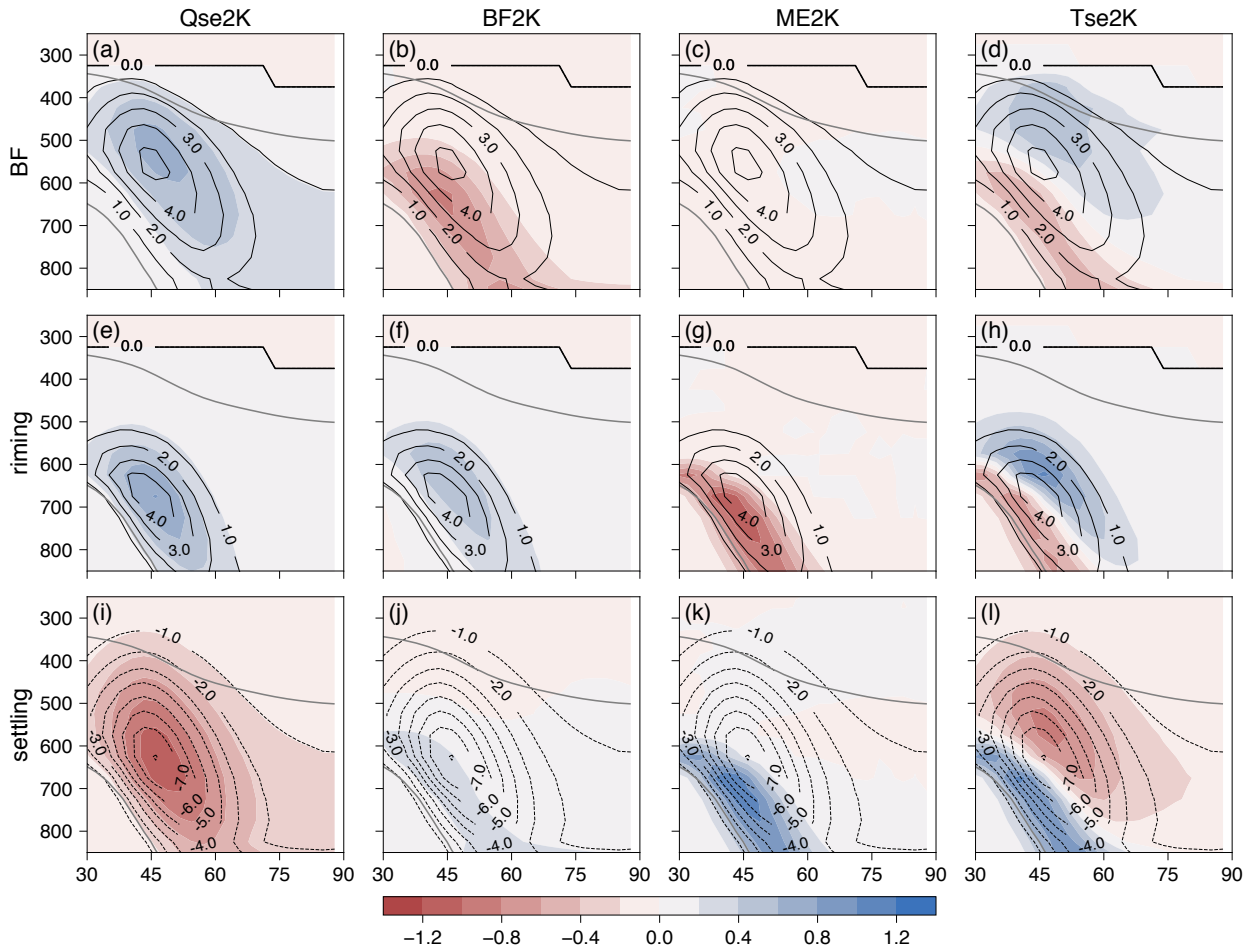
704 FIG. 3. Normalized changes in the zonal-mean extratropical LWP (the upper panels) and IWP (the lower  
 705 panels) ( $\text{g m}^{-2} \text{K}^{-1}$ ) in the process-level experiments.



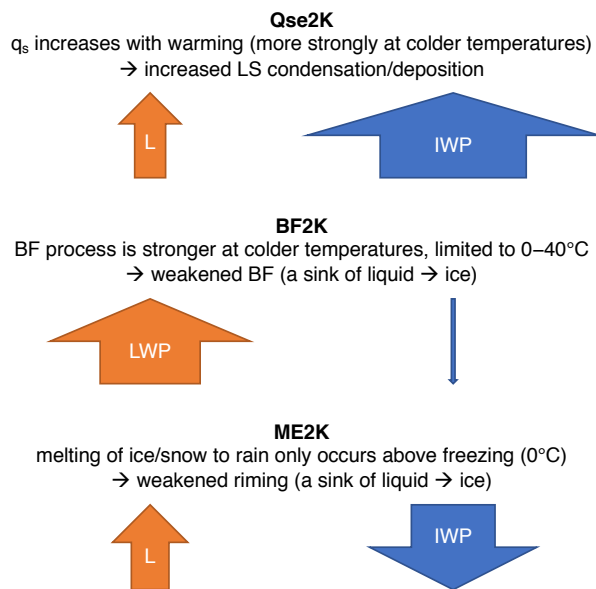
706 FIG. 4. Vertical distributions of the normalized changes in the zonal-mean mixing ratios of cloud liquid and ice  
 707 ( $10^{-6} \text{ kg kg}^{-1} \text{ K}^{-1}$ ) in the key process-level experiments. Differences between the perturbation and Ctrl runs are  
 708 shown as colored shading. Ctrl run values are depicted by the contours with a spacing of  $5 \cdot 10^{-6} \text{ kg kg}^{-1}$ . Thick  
 709 grey lines show the  $0^\circ\text{C}$  and  $-40^\circ\text{C}$  isotherms. The x- and y-axes are latitude and pressure (hPa), respectively.



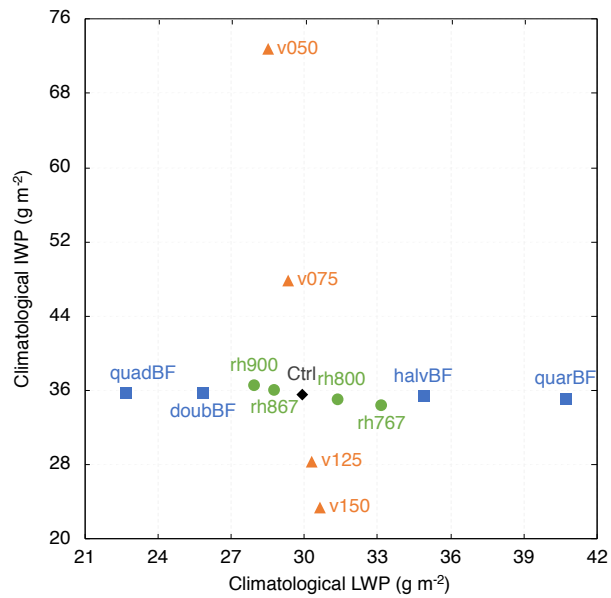
710 FIG. 5. Vertical distributions of the normalized changes in the zonal-mean time tendency terms of cloud liquid  
 711 mixing ratio ( $10^{-9} \text{ kg kg}^{-1} \text{ s}^{-1} \text{ K}^{-1}$ ) in the key process-level experiments. Differences between the perturbation  
 712 and Ctrl runs are shown as colored shading where a positive value indicates an increase in cloud liquid tendency.  
 713 Ctrl run values are represented by the contours with a spacing of  $1 \cdot 10^{-9} \text{ kg kg}^{-1} \text{ s}^{-1}$ . The tendency terms shown  
 714 are condensation, autoconversion, accretion, the BF process, and riming. Thick grey lines are the  $0^\circ\text{C}$  and  $-40^\circ\text{C}$   
 715 isotherms. The x- and y-axes are latitude and pressure (hPa), respectively.



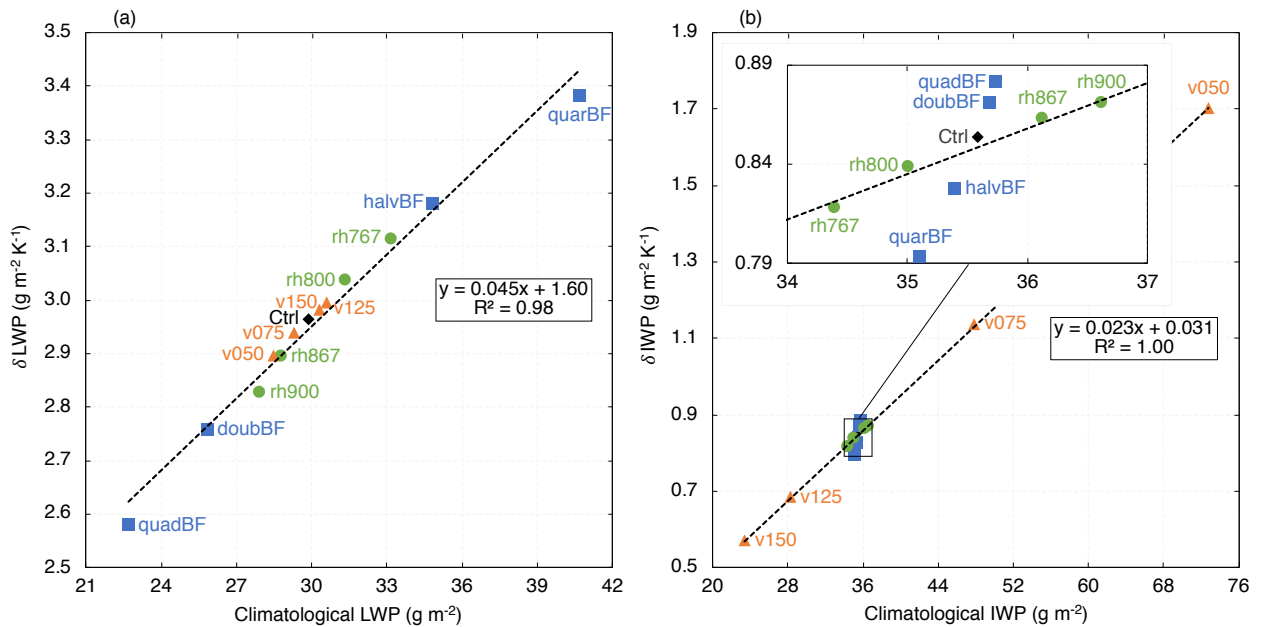
716 FIG. 6. As Fig. 5 but for cloud ice instead of cloud liquid, with tendency terms shown being the BF process,  
 717 riming, and gravitational ice settling.



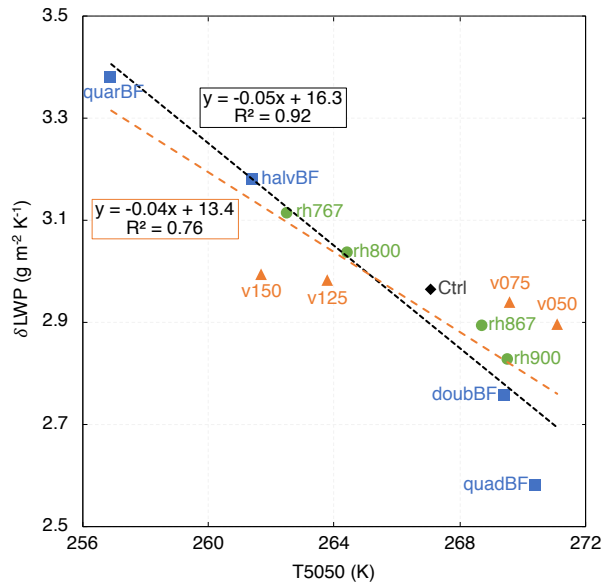
718 FIG. 7. Summary of the three main processes (highlighted by Qse2K, BF2K, and ME2K experiments)  
 719 underlying the LWP/IWP feedback. Arrow width and direction represent the relative magnitude and sign  
 720 (upward denoting an increase) of the LWP/IWP changes, respectively.



721 FIG. 8. Climatological LWP ( $\text{g m}^{-2}$ ) plotted against the climatological IWP ( $\text{g m}^{-2}$ ) in the perturbed parameter  
 722 experiments.



723 FIG. 9. Normalized changes in LWP/IWP ( $\text{g m}^{-2} \text{K}^{-1}$ ) in the full warming (Tse2K) experiments plotted against  
 724 the climatological LWP/IWP ( $\text{g m}^{-2}$ ) in the perturbed parameter experiments. Panels (a) and (b) are for LWP  
 725 and IWP, respectively. The rectangle in Panel (b) is a blowup of the data points clustered around Ctrl.



726 FIG. 10. Normalized changes in LWP ( $\text{g m}^{-2} \text{K}^{-1}$ ) in the full warming (Tse2K) experiments plotted against  
 727 the climatological T5050. The black and orange dotted lines represent the best linear fits without and with the  
 728 ice fall speed experiments, respectively.